Journal of Physics and Chemistry of Solids 96-97 (2016) 83–91

Contents lists available at ScienceDirect

Journal of Physics and Chemistry of Solids

journal homepage: www.elsevier.com/locate/jpcs

Morphological evolution and visible light-induced degradation of Rhodamine 6G by nanocrystalline bismuth tungstate prepared using a template-based approach

Raissa Mendes Silva [a], Diego Augusto Batista Barbosa [a], Caritas de Jesus Silva Mendonça [a], José Renato de Oliveira Lima [a], Fernando Carvalho Silva [a], Elson Longo [c], Adeilton Pereira Maciel [a], Carlos William de Araujo Paschoal [b], Marcio Aurélio Pinheiro Almeida [a,*]

[a] *Centro de Ciências Exatas e Tecnologia, Universidade Federal do Maranhão, 65080-805, São Luís, MA, Brazil*
[b] *Departamento de Física, Universidade Federal do Ceará, Campus do Pici, 65455-900, Fortaleza, CE, Brazil*
[c] *Instituto de Química, UNESP – Universidade Estadual Paulista, 14800-900 Araraquara, SP, Brazil*

ARTICLE INFO

Article history:
Received 23 November 2015
Received in revised form
11 March 2016
Accepted 6 May 2016
Available online 7 May 2016

Keywords:
Bi_2WO_6
Surfactants
Photodegradation

ABSTRACT

The cleaning of water contaminated with organic dyes is a crucial problem nowadays. The search for good catalysts is intense, and bismuth tungstates have attracted a lot of attention because of their catalytic properties which are related to their crystal structure and morphology. In this study, we show that Bi_2WO_6 (BWO) crystals synthesized by the surfactant-assisted hydrothermal method create a different morphology than non-assisted crystals. With the assistance of the PVP surfactant, even the BWO crystalline structure could change, crystallizing into a high-symmetry metastable phase. These changes in morphology imply a decrease in BWO catalytic activity, which shows that insightful control of BWO synthesis is necessary to improve the BWO properties.

1. Introduction

Contamination of river water is a major problem in modern society. In recent years, the effluent water contaminated with organic molecules is a great concern. Organic dyes are toxic, potentially carcinogenic, and not biodegradable, which can lead to serious environmental and animal health problems [1]. Moreover, these dyes directly affect the photosynthesis rate due to poor light penetration in aquatic systems, which can cause a decrease in oxygen content and result in fish death.

The advanced oxidation processes (AOP) is a potential alternative for the treatment of water contaminated with organic dyes [2–5]. Combining irradiation with catalysts (oxides), both homogeneous (photo-Fenton process) [6] and heterogeneous [7,8] catalysis, has attracted considerable attention due to efficient organic compound degradation [9]. In this approach, transition metal oxides have largely been studied [10–15], with titanium dioxide [5,9] and other titanium doped oxides [15–18] being some of the most investigated. Bismuth oxides and derivatives show enormous potential in remediating environments contaminated by organic or inorganic pollutants [19–21].

In particular, tungstates, which constitute another class of metal oxides, are very promising for such applications [22–24]. In particular, bismuth tungstates have attracted attention in the research of nanostructured materials because of their applications as catalysts [25–29]. Bi_2WO_6 (BWO) has an orthorhombic structure with $P2_1ab$ space group and belongs to the Aurivillius family of compounds. These compounds have a general formula of $(Bi_2O_2)^{2+}$ $(A_{n-1}B_nO_{3n-1})$, where A represents a mono-, bi-, or trivalent ion; B denotes a tetra-, penta-, or hexavalent ion; and n is the BO_6 octahedra number in each pseudo-perovskite block [30]. Many papers have described structural change as a key factor in the enhancement of catalytic properties [19,20]. Therefore, various synthesis methods have been used to obtain new structured materials to enhance the BWO properties [31–33].

The template method, using templates such as ethylene glycol (EG) [34], cetyltrimethylammonium bromide (CTAB) [35], and glycine (gly) [36], has been widely used to promote structural changes in BWO. The compounds obtained in the presence of

---

* Corresponding author.
E-mail addresses: paschoal.william@gmail.com, paschoal.william@fisica.ufc.br (C.W. de Araujo Paschoal), almeida.pinheiroa@gmail.com (M.A.P. Almeida).

http://dx.doi.org/10.1016/j.jpcs.2016.05.004

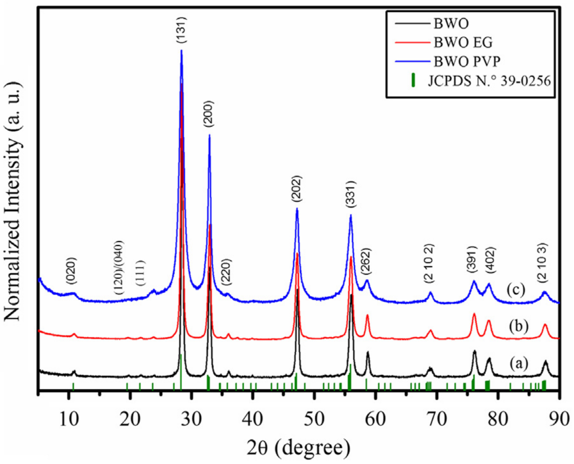

Fig. 1. XRPD patterns of Bi_2WO_6 (BWO) crystals. (a) Conventional BWO crystal. (b) BWO-EG and (c) BWO-PVP BWO crystals synthesized using EG and PVP surfactants, respectively.

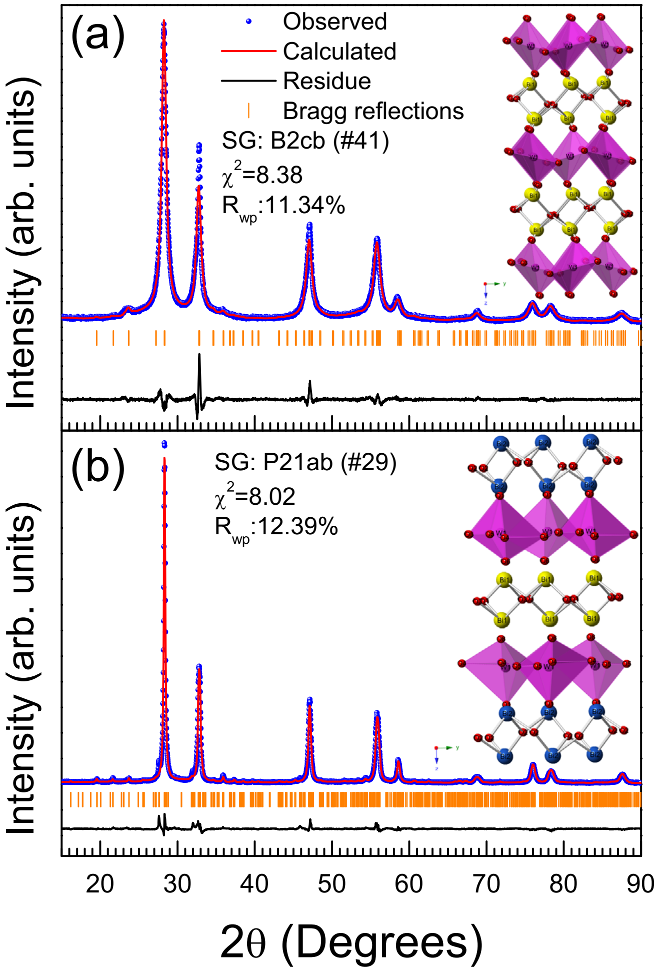

Fig. 2. Refined XRPD patterns for (a) PVP-based BWO crystals and (b) non-surfactant crystals. The insets show the refined crystalline structure for non-surfactant (inset in (a) and PVP-based BWO (inset in (b)) crystals.

these organic molecules show significant changes in the investigated properties. However, such changes, particularly changes in the photocatalytic properties, are still not well understood, especially when structural changes are involved. In this study, we describe the synthesis of the BWO crystal by the template method and correlate its properties with its structure and morphology.

2. Experimental details

2.1. Sample preparation

The samples were prepared using the surfactant-assisted hydrothermal method with ethylene glycol (EG) and poly(4-vinylpyridine) (PVP 60) as surfactants. In this method, 0.01 mol of sodium tungstate dihydrate [($Na_2WO_4 \cdot 2H_2O$), 99% purity, Aldrich] and 0.02 mol of bismuth nitrate [$Bi(NO_3)_3$, 99% purity, Aldrich] were added to 100 mL of each surfactant solution (5% EG and 5% PVP 60). This mixture was stirred for 10 min and the suspension was transferred into a Teflon autoclave, which was sealed and kept at 180 °C for 12 h. Yellow crystals [Bi_2WO_6 (BWO)] were obtained; the crystals were dried on a hot plate at 50 °C for 8 h. Thus, two samples were obtained (corresponding to each surfactant) and labeled BWO-EG and BWO-PVP.

2.2. Crystal characterization

The crystalline structure was investigated by X-ray powder diffraction (XRPD) using a Rigaku-DMax/2500PC (Japan) with Cu-Kα radiation ($\lambda = 1.5406$ Å) in the 2θ range of 5° to 100° with a scanning rate of 0.02°/min. The crystals' shape and size were analyzed by field emission scanning electron microscopy (FEG-SEM) using a Carl Zeiss model Supra 35-VP (Germany) operated at 6 kV. Raman spectroscopy measurements were performed on a Horiba spectrometer model iHR550 coupled to an Olympus BX30 microscope. The Raman signal was excited by a He–Ne laser ($\lambda = 630$ nm) and acquired in a backscattering configuration. The optical features of the spectrometer were setup to achieve a resolution of up to 2 cm^{-1}. FT-IR spectra were recorded on a Bomem-Michelson spectrophotometer in transmittance mode (Model MB-102) in the 250 to 1,200 cm^{-1} range using KBr pellets. Ultraviolet–visible (UV–vis) spectra were obtained using a Varian spectrophotometer model Cary 5G (USA) operating in the diffuse refection mode. All measurements were performed at room temperature.

2.3. Photocatalytic activity

The crystal's photocatalytic activities were evaluated by the degradation of rhodamine 6G (Rh 6G) under artificial solar-light. In a typical experiment, 0.1 g of photocatalyst was dispersed into 100 mL of Rh 6G solution (1×10^{-5} mol/L). A 500 W Xe lamp was used to simulate solar-light irradiation. Illumination was conducted after the suspensions were stirred in the dark for 30 min to ensure the establishment of an adsorption–desorption equilibrium between the photocatalyst and dye. At certain time intervals, 5 mL of the suspension was taken from the vessel and centrifuged immediately. The filtrate was analyzed to measure the absorbance of Rh 6G at 553 nm using a double-beam UV–vis spectrophotometer (JASCO Modelo V-660, US).

3. Results and discussion

3.1. XRD patterns and Rietveld refinement analyses

Fig. 1 shows the XRPD diffractograms obtained for BWO crystals based on both surfactants, EG and PVP. For the sake of comparison, the XRPD pattern of the conventional BWO single crystal, obtained by the hydrothermal method without surfactant, is also presented in Fig. 1. Clearly, we successfully obtained BWO single crystals with both surfactants since the obtained samples exhibit XRPD patterns characteristic of crystalline BWO. For the conventional and EG-based sample (BWO-EG), diffraction peaks were indexed to the

Table 1
Refined structural data for PVP-based (*B2cb* structure) and pure BWO crystals ($P2_1ab$ structure), respectively.

B2cb structure										
Cell parameters: a=5.459(5) Å b=5.461(5) Å c=16.386(15) Å; Cell volume 488.49(77) Å^3										
Bonds				Fractional coordinates						
Atom 1	Atom 2		Bond distance (Å)	Label	Wyckoff site	*x*	*y*	*z*	Occ.	Uiso
Bi1	O2	1 ×	2.0643(1131)	Bi1	8b	−0.427(8)	0.5262(11)	0.1712(5)	1	0.0515
	O2	1 ×	2.1614(1261)	W1	4a	−0.400(8)	0	0	1	0.0459
	O2	1 ×	2.4167(1123)	O1	8b	0.008(18)	0.046(17)	0.125(6)	1	0.025
	O2	1 ×	2.6980(1212)	O2	8b	0.309(16)	0.281(31)	0.7655(31)	1	0.025
				O3	8b	0.131(14)	0.675(12)	0.974(5)	1	0.025
W1	O1	2 ×	3.0363(1034)							
	O3	2 ×	1.0599(691)							
	O3	2 ×	3.1443(814)							
$P2_1ab$ structure										
Cell parameters: a=5.4411(3) Å b=5.4594(4) Å c=16.4325(10) Å; Cell volume 488.13(5) Å^3										
Bi1	O3	1 ×	2.1770(1185)	Bi1	4a	−0.026(4)	0.5198(11)	0.42595(31)	1	0.0393
	O3	1 ×	2.1813(1283)	Bi2	4a	−0.012(4)	0.4855(9)	0.07994(30)	1	0.0378
	O3	1 ×	2.2408(1346)	W1	4a	0.003(5)	0.0101(28)	0.2508(6)	1	0.0336
	O3	1 ×	2.5501(1357)	O1	4a	0.168(8)	0.012(14)	0.1119(30)	1	0.025
				O2	4a	0.272(16)	0.315(28)	1.009(5)	1	0.025
Bi2	O2	1 ×	2.1478(1027)	O3	4a	0.246(17)	0.216(33)	0.502(5)	1	0.025
	O2	1 ×	2.1688(1065)	O4	4a	0.391(19)	0.528(25)	0.268(5)	1	0.025
	O2	1 ×	2.3306(1238)	O5	4a	0.482(29)	0.361(13)	0.254(6)	1	0.025
	O2	1 ×	2.7856(1187)	O6	4a	0.519(15)	0.535(10)	0.3560(24)	1	0.025
W1	O4	1 ×	0.7032(1065)							
	O5	1 ×	0.7149(763)							
	O6	1 ×	1.7483(412)							
	O1	1 ×	2.4527(504)							
	O5	1 ×	3.235(136)							
	O4	1 ×	3.3859(1260)							

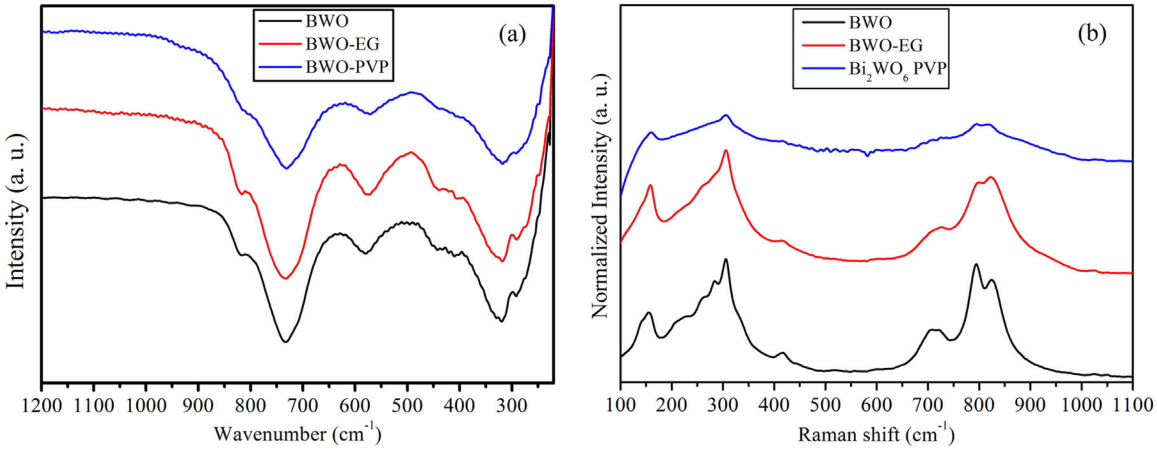

Fig. 3. (a) FT-IR spectra and (b) Raman spectra as-synthesized samples.

pure and the orthorhombic phase of BWO according to Joint Committee on Powder Diffraction Standards (JCPDS) card no. 39-0256 [37]. No impurity could be found under the limit of resolution used in the XRPD measurements.

However, we observed that peaks associated with the (120) and (040) crystallographic planes were absent in PVP-based BWO crystals, which indicates that this sample has a slightly different structure. Also, the peak associated to the (111) plane in this sample changes. Due to the small changes, the new structure is probably symmetry-related to the usual BWO $P2_1ab$ orthorhombic phase.

In addition, the diffraction peaks of the surfactant-based samples were broader than that without the surfactant, which implies that the particle size was reduced. The obtained crystals had nanometric sizes, which is usual when using this synthesis method. This assumption about the size will be confirmed later by microscopy measurements.

Fig. 2 shows the refined diffractograms of the BWO-PVP and calcinated BWO-PVP samples. Both structures were refined using the orthorhombic crystal system, and the obtained structures belong to the *B2cb* and $P2_1ab$ space groups, respectively. The transition of BWO-PVP from *B2cb* to $P2_1ab$ space group after calcination is indicated by the presence of the (120), (040), and (111) reflections around 20–25°, which are more intense in the former space group. The $P2_1ab$ space group is usually observed at room temperature, while the *B2cb* is a higher symmetry phase observed at high pressures and temperatures [38,39]. The *B2cb* structure occurs with the loss of octahedral tilt around the *c* axis in the WO_4

Table 2
Main Raman-active modes assignment for the obtained BWO in symmetry $P2_1ab$. Symmetry is related to the tetragonal phase.

Observed (cm^{-1})	Symmetry	Modes	Ref.
90	E_g	Translational modes of Bi and W	[43]
100	E_g	Translational modes of Bi and W	[43]
140	A_{1g}	Translational modes of Bi and W	[43]
150	A_{1g}	Translational modes of Bi and W	[43]
180	E_g	Translational modes of Bi and W	[43]
210	A_{1g}	Bendings of WO_6 and $(Bi_2O_2)^{2+}$	[39]
230	E_g	Bendings of WO_6 and $(Bi_2O_2)^{2+}$	[39]
260	E_g	Bendings of WO_6 and $(Bi_2O_2)^{2+}$	[39]
280	E_g	Bendings of WO_6 and $(Bi_2O_2)^{2+}$	[39]
310	E_g	Bendings of WO_6 and $(Bi_2O_2)^{2+}$	[39]
335	E_u	Bendings of WO_6 and $(Bi_2O_2)^{2+}$	[39]
360	E_u	Bending of $(Bi_2O_2)^{2+}$	[41]
410	E_u	Bending of WO_6 (mainly equatorial Oxygens)	[41]
420	E_u	Bending of WO_6 (mainly equatorial Oxygens)	[41]
450	A_{2u}	Bending of $(Bi_2O_2)^{2+}$	[41]
520	A_{2u}	Bending of WO_6 (mainly equatorial Oxygens)	[41]
600	A_{2u}	Bending of WO_6 (mainly equatorial Oxygens)	[41]
700	E_u	Asymmetric stretching of WO_6 (mainly equatorial Oxygens)	[41]
720	E_u	Asymmetric stretching of WO_6 (mainly equatorial Oxygens)	[41]
800	A_{1g}	Symmetric stretching of WO_6 (mainly apical Oxygens)	[41]
830	A_{2u}	Asymmetric stretching of WO_6 (mainly apical Oxygens)	[41]

perovskite-like layer. The *B2cb* structure has only one Bi and three O nonequivalent atoms, while the $P2_1ab$ structure has two Bi and six O nonequivalent atoms. Table 1 shows the bond distance for all nonequivalent atoms. Due to several bonds with different distances, the $P2_1ab$ structure is more distorted than *B2cb*.

3.2. FT-IR and Raman spectroscopy analyses

FT-IR and Raman spectra are shown in Fig. 3(a) and (b). The BWO and BWO-EG samples both exhibit IR and Raman spectra typical of orthorhombic BWO crystals, confirming the XRPD result. In the $Pca2_1$ structure, according to the crystal site occupations, BWO crystals exhibit 105 optical modes. All of these modes are Raman-active ($\Gamma^{\text{Raman}}=26A_1+27A_2+26B_1+26B_2$ in terms of the irreducible representations of the mm2 factor group) and 78 are IR-active ($\Gamma^{\text{IR}}=26A_1+26B_1+26B_2$). These modes can be assigned into symmetric and asymmetric stretching and bending modes of the molecular WO_6 octahedra and the $(Bi_2O_2)^{2+}$ layer, as well as the Bi^{3+} and W^{6+} ion translations.

In FT-IR spectra (Fig. 3(a)), we observed both asymmetric and symmetric WO_6 stretching modes at around 820 and 750 cm^{-1}. The bands in the 480–620 cm^{-1} region correspond to WO_6 bending vibrations, while the vibration modes at 320 cm^{-1} are indicative of WO_6 bending. The low wavenumber modes (below 320 cm^{-1}) correspond to the $(Bi_2O_2)^{2+}$ bending modes [40,41]. In the mid-IR range of the spectrum, all three samples have similar spectra because we are observing mainly the molecular modes. Since we used KBr pellets, the precise positions of the phonons below 400 cm^{-1} should be slightly distorted, so we discussed the phonons below this wavenumber only in terms of their ranges.

Fig. 3(b) shows the Raman spectra of the samples. In BWO and BWO-PVP, we observed three well-defined modes (710, 800, and 830 cm^{-1}), which is attributed to the WO_6 asymmetric (710 and 830 cm^{-1}) and symmetric (800 cm^{-1}) stretching modes [41]. In the middle range of the spectra, from 250 to 400 cm^{-1}, we observed in- and out-of-plane WO_6 deformations (280, 310, and 420 cm^{-1}) [42]. At low-wavenumber modes from 150 to 230 cm^{-1}, we observed Bi^{3+} ion translation [39].

The BWO-PVP sample has a broad Raman spectrum. This feature originates from a structural phase transition induced by the surfactant presence during the synthesis. Thus, a metastable *B2cb* structure is induced since the Raman spectrum of this sample is characteristic of the phase [38,41,43].

From the spectra, we observed 11 phonons in PVP-based BWO crystals from 140 to 850 cm^{-1}. Conversely, we observed these 11 phonons in the other samples (EG and non-surfactant based samples), in the range 80–350 cm^{-1}. A detailed assignment of the observed phonons is shown in Table 2, where we inserted the phonons symmetries in tetragonal phase for completeness. All spectra are in agreement with those obtained by Maczka et al. [43] including the broadening observed in BWO-PVP sample.

To show that the *B2cb* phase is induced by the PVP-assisted synthesis, we get a fraction of this sample, heat it up to 600 °C for 4 h, and decrease the temperature slowly to permit the system to follow the most conventional low energetic phase. Fig. 4 shows the XRPD pattern and Raman spectra for a BWO-PVP sample before and after the thermal treatment. Pure BWO samples are showed for the sake of comparison. In Fig. 3(a), the XRPD pattern of thermal treated BWO-PVP sample is similar to a conventional BWO sample, which suggests that after the thermal treatment the BWO-PVP sample stabilizes the $P2_1ab$ phase confirming the *B2cb* is a metastable phase. This assumption is strongly evidenced by the Raman spectroscopy seen in Fig. 4(b), which is very sensible to local symmetries. The BWO-PVP Raman spectrum is undoubtedly characteristic of a $P2_1ab$ structure. Therefore, the *B2cb* exhibited by the BWO-PVP sample is metastable at room temperature and was induced by the PVP surfactant present during the hydrothermal synthesis.

3.3. Morphological evolution of the BWO nanostructures

Fig. 5(a)–(d) shows the FE-SEM BWO crystals micrographs. In the absence of the surfactant, the obtained BWO crystals seen in Fig. 4(a) have a cabbages-like morphology ranging from 3000 to 3500 µm. Conversely, crystals obtained in the surfactant presence (BWO-EG and BWO-PVP) have morphological units of a dramatically reduced size. While BWO-EG exhibits nanoplate-like crystals of approximately 50–150 nm (Fig. 4(b)), BWO PVP (Fig. 4(c)) shows a mix of morphology rods-like and flower-like crystals.

The presence of a surfactant influences the BWO crystals microstructure. The crystal growth, which is guided by the high-energy surfaces, starts after the formation of the first crystallites. At this time, the PVP large chain surfactant molecule, which has been interacting with the ions (Bi^{3+}, ${WO_4}^{2-}$) since the micelles formation, leads to the rod formation, which is facilitated by the interaction of the electron pair of the pyridine group with the highest energy surfaces.

3.4. UV–vis diffuse reflectance spectroscopy

From the UV–vis spectra we can estimate the band gap (E_g) of BWO crystal using the Tauc equation [44], in which the band gap E_g is given by formula $(\alpha h\nu)=A(h\nu-E_g)^n$, where h is the Planck's constant, ν is the frequency, α is the absorption coefficient, and A is proportionality constant. The variable n can be 1/2, 3/2, 2, or 3 for allowed direct, forbidden direct, indirect allowed, and indirect forbidden transitions, respectively [45,46]. The bandgap can be estimated with the Kubleka–Munk method, which calculates the absorption coefficient using the following formula,

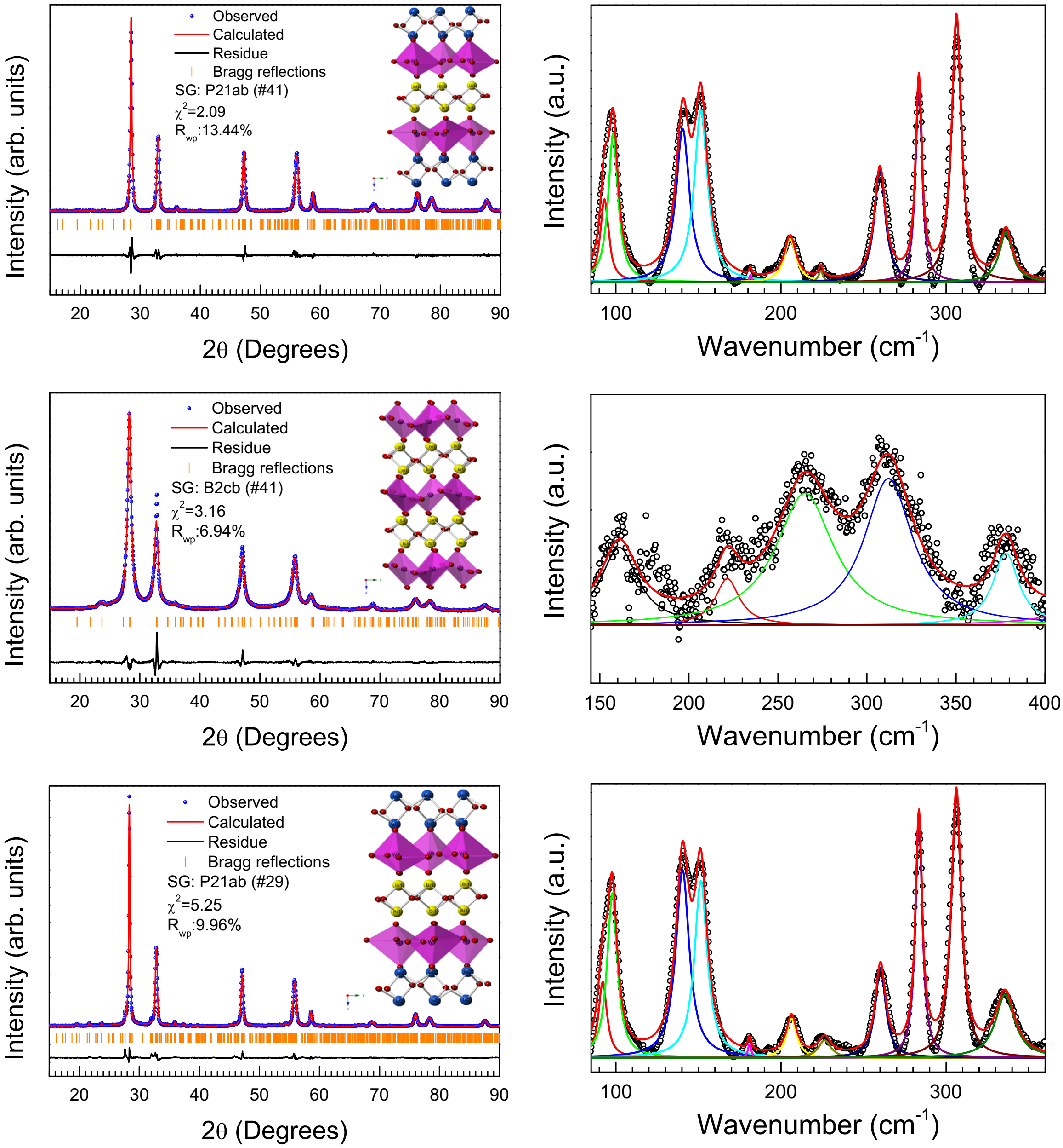

Fig. 4. XRPD (left) patterns and Raman spectra for pure BWO (bottom), BWO-PVP (middle) and BWO-PVP thermally treated (top).

$$\frac{k}{s} = \frac{(1-R_{\infty}^{2})}{2R_{\infty}} = F(R_{\infty})$$

where R_{∞} is the reflectance, s is the scattering coefficient, k is the molar absorption coefficient, and $F(R_{\infty})$ is the Kubleka–Munk function. Thus, the vertical shaft can be converted to $F(R_{\infty})$, which is proportional to the absorption coefficient. Therefore, in the Tauc equation, α can be replaced by $F(R_{\infty})$ and produce an estimated value of E_g using the following formula $[F(R_{\infty})h\nu]=A(h\nu-E_g)^n$. Using the Kubelka–Munk function $(h\nu F(R_{\infty}))$, is possible to plot against the $h\nu$. The band gap can be obtained by extrapolating to zero the linear fit of the curve obtained $((h\nu F(R_{\infty}))^n$ versus $h\nu)$, which is often called Tauc extrapolation [47,48]. According to the literature, BWO has an allowed direct transition [27,49].

Fig. 6 shows the Tauc plots for all samples. We can observe the BWO band gap change with surfactant presence. While BWO-EG has a slightly reduced bandgap (3.06 eV) when compared to conventional BWO (3.17 eV), BWO-PVP crystals have a large bandgap (3.41 eV) when compared with conventional BWO crystals. The small E_{gap} values can be related to the presence of intermediary energy levels within the band gap of BWO crystals. These energy levels are dependent on the structural order degree in the orthorhombic lattice. Thus, our results indicate that BWO-PVP presents large structural order degree when compared with the other samples. These observations are expected since a change structural derived from of $P2_1ab$ to $B2cb$ symmetry was observed in the Raman spectra [38].

Determining the band gaps is crucial since they are approximately the same energy required to promote electrons of the valence band to the conduction band. This promotion results in the formation of oxidizing species that are responsible for the catalysis process.

3.5. Photocatalytic activity

Kinetic studies using photocatalysis BWO samples were carried out applying the pseudo-first order, as expressed in equation −ln

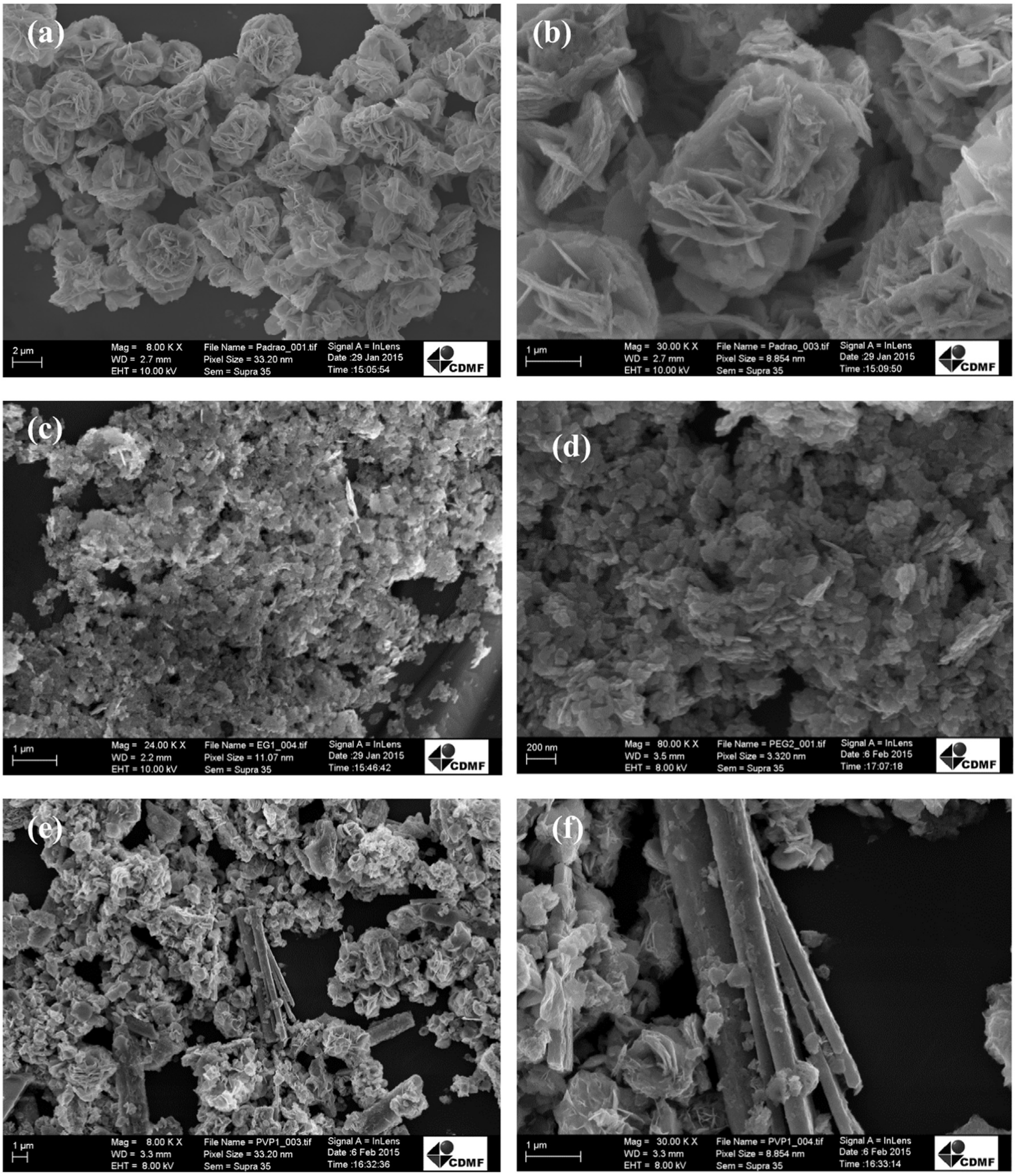

Fig. 5. Selected FE-SEM micrographs for BWO sample: (a,b) conventional BWO, (c,d) BWO EG and (e,f) BWO PVP.

$(C/C_0)=kt$, where C_0 and C are the initial and time t Rh 6G dye concentrations in the solution, respectively, and k is the rate constant generally used for this type of catalytic degradation process [49].

Fig. 7 shows the UV–vis spectra for the degradation of Rh 6B through the BWO samples. After approximately 120 min, we can observe that 95% of the dye was degraded. Moreover, there is a small shift of the absorption band to larger energies during the degradation. The band shift indicates the beginning of degradation. In the dye degradation process, electronic density donor groups are first removed creating a low donor concentration, which results in a band shift to higher energies. This result is in agreement with other previous works [10,13].

Fig. 8 shows the decay curve for the Rh 6G dye degradation. The BWO conventional sample had more photocatalytic efficiency than the BWO-EG and BWO-PVP samples since they have slower degradation kinetics at 60 and 50% after 120 min of irradiation, respectively. While conventional BWO samples exhibit a catalysis rate constant (k) of 0.028 min^{-1}, BWO EG and BWO PVP exhibited 0.008 min^{-1} and 0.007 min^{-1}, respectively.

Although we got reduced-size particles, these changes were not sufficient for an improvement in the catalytic activity. These results are in agreement with the large band gap obtained for the BWO-PVP sample. High bandgap values make it difficult to promote valence band electrons to the conduction band forming e^-/h^+ pairs, which are responsible for the oxidizing species formation. This is consistent with the BWO sample having a greater kinetic degradation of Rh 6G dye when using irradiation of 370 nm (3.35 eV). However, the BWO-EG sample has a lower bandgap and also exhibited low catalytic activity. A possible explanation for this

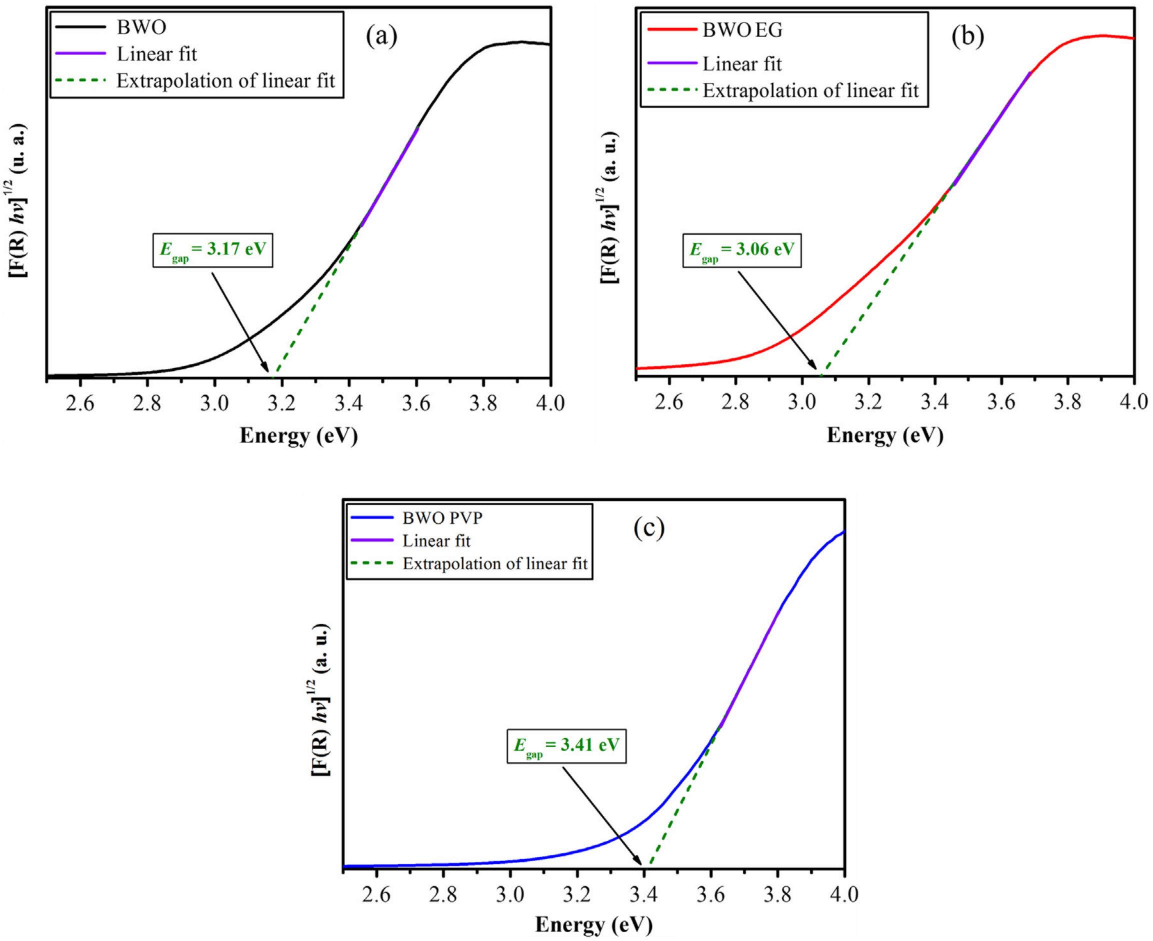

Fig. 6. UV–vis diffuse reflectance spectra of the BWO sample. a) BWO, b) BWO-EG, and c) BWO-PVP.

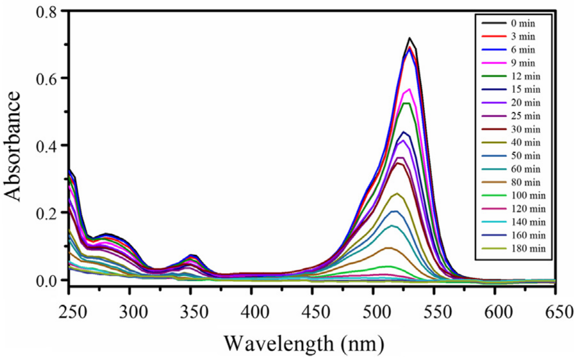

Fig. 7. Temporal evolution of the Rh 6G absorption spectra in the BWO presence BWO.

occurrence could be the greater recombination rate since this event decreases the amount of oxidizing species such as hydroxyl radicals, superoxides, and singlet oxygens, which are molecules responsible for dye degradation [13,50–52].

With the change in the symmetry of the compound, various defects were created. This assertion is consistent with the Rietveld refinement analyses since the structure obtained with PVP is distorted with elongated bindings, which result in a change of morphology. We proved that the *B2cb* symmetry, which had rod-like morphology, did not have a good catalytic activity proving the $P2_1ab$ symmetry is more appropriate, which is also reflected in a lower value band gap, 3.17 eV. Therefore, we emphasize that the change in morphology is a key factor for the catalytic activity, which is directly linked to the structural changes responsible for variations in band gap and catalytic sites.

To analyze the Rh 6G degradation mechanism, we added in catalytic reaction scavengers of oxidative species, such as isopropyl alcohol (IPA), benzoquinine (BQ), silver nitrate ($AgNO_3$), and sodium oxalate (NaC_2O_4), which are responsible for the capture of $OH^{-\bullet}$, $O_2^{-\bullet}$, e^-, and h^+ species in the solution, respectively [53]. Furthermore, to confirm that the oxygen adsorbed on the catalyst surface is important in the catalytic process, the experiment was carried out under nitrogen atmosphere. Both results are shown in Fig. 9. With the addition of isopropyl alcohol, the rate constant observed was approximately 0.020 min^{-1}. However, when the benzoquinone was added, the rate constant was reduced to 0.0065 min^{-1}. This value suggests that the responsible species for the dye oxidation is a superoxide radical. When the catalysis was carried out in nitrogen saturated solution, there was a reduction in the constant rate (Fig. 9b). The same was observed with catalysis involving silver nitrate and sodium oxalate additions. This result shows the oxygen adsorbed on the BWO surface reacts with the valence band promoted electrons, which is responsible by the dye degradation. Therefore, this mechanism, which is described by the Eqs. (1)–(3), is schematically depicted in Fig. 10.

4. Conclusions

We successfully obtained BWO nanocrystals by the PVP and EG surfactant-assisted hydrothermal method. Non-assisted BWO and PVP-assisted BWO crystals crystallized into the conventional

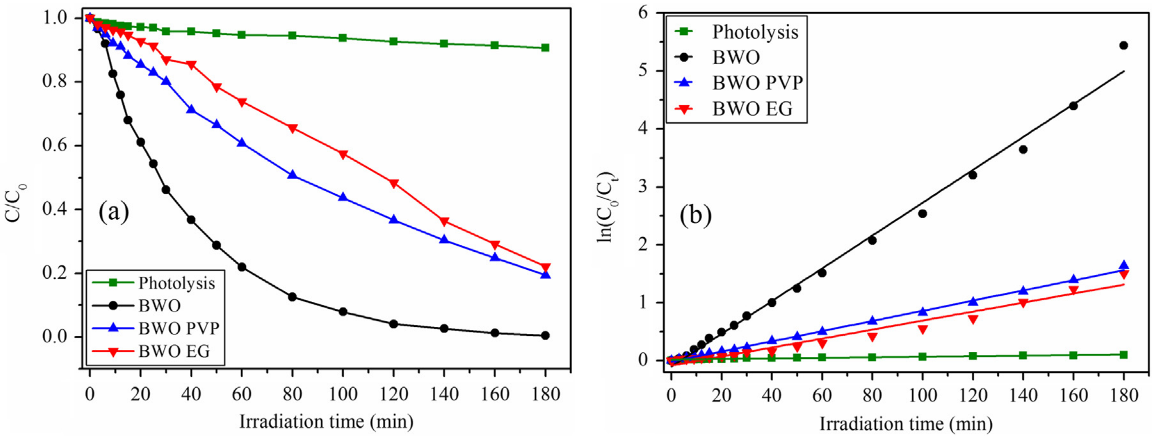

Fig. 8. (A) Photocatalytic Rh 6G degradation of by different BWO photocatalysts under visible-light irradiation. (B) Relation between ln(C/C_0) and irradiation time for BWO samples and photolysis.

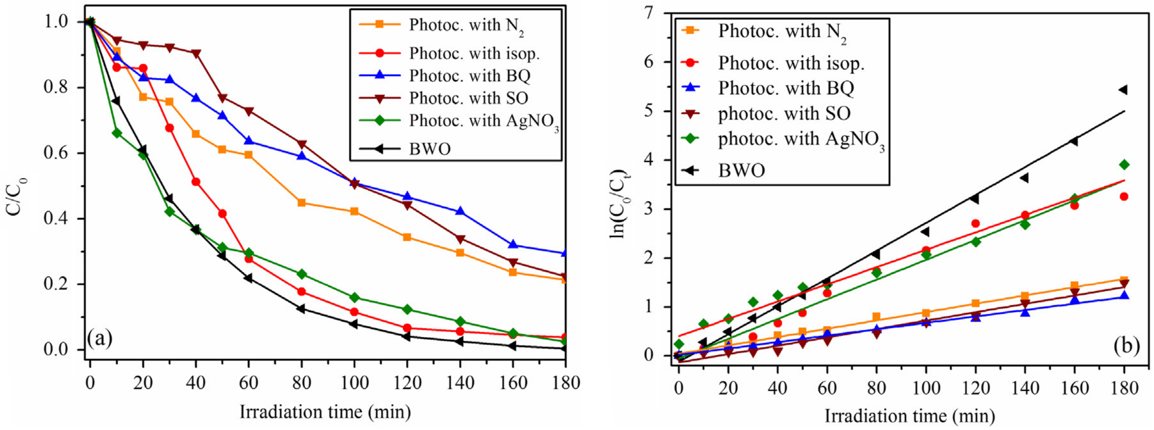

Fig. 9. Effect of different scavengers on the degradation of Rh 6G in the presence of photocatalyst. a) Decay curve for Rh 6G degradation using scavengers. b) Degradation kinetics for Rh 6G using scavengers.

$$Bi_2WO_6 + h\nu \rightarrow Bi_2WO_6 + (e^-_{CB} + h^+_{VB}) \quad (1)$$

$$e^-_{CB} + O_2 \rightarrow O_2^{\cdot -} \quad (2)$$

$$O_2^{\cdot -} + \text{Rh 6G} \rightarrow \textit{degraded products} \quad (3)$$

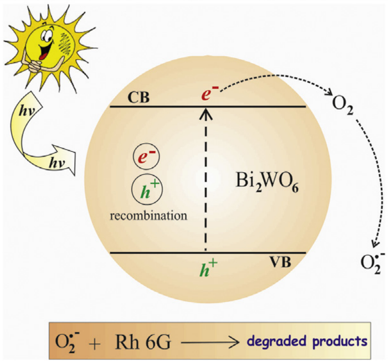

Fig. 10. Schematic illustration for processes of separation and transfer of photo-generated charge carriers in BWO for organic dye degradation simulated by light.

orthorhombic $P2_1ab$ structure. The PVP-BWO sample crystallized in a metastable phase *B2cb* high-symmetry phase as observed by XRPD measurements and confirmed by Raman spectroscopy. Both samples have lower photocatalytic activity than non-assisted BWO crystals, which can be explained by the EG an PVP-based BWO crystals shapes.

Acknowledgments

The authors acknowledge the financial support of the Brazilian research financing institutions FAPEMA (N°. 03965/15 and 00563/15), CNPq (including PIBIC) and CAPES.

References

[1] Z.J. Zhang, W.Z. Wang, J. Ren, J.H. Xu, Appl. Catal. B – Environ. 123 (2012) 89–93.
[2] D. Ravelli, D. Dondi, M. Fagnoni, A. Albini, Chem. Soc. Rev. 38 (2009) 1999–2011.
[3] M.R. Hoffmann, S.T. Martin, W.Y. Choi, D.W. Bahnemann, Chem. Rev. 95 (1995) 69–96.
[4] M.A. Fox, M.T. Dulay, Chem. Rev. 93 (1993) 341–357.
[5] A. Fujishima, T.N. Rao, D.A. Tryk, J. Photochem. Photobiol. C: Photochem. Rev. 1 (2000) 1–21.
[6] A.C. Pradhan, B. Nanda, K.M. Parida, M. Das, Dalton Trans. 42 (2013) 558–566.
[7] C.Y. Wu, Y.T. Liu, P.C. Huang, T.J.M. Luo, C.H. Lee, Y.W. Yang, T.C. Wen, T.Y. Chen, T.L. Lin, Nanoscale 5 (2013) 9181–9192.
[8] Q. Zhang, H.Y. Wang, X.L. Jia, B. Liu, Y.H. Yang, Nanoscale 5 (2013) 7175–7183.
[9] R.S. Thakur, R. Chaudhary, C. Singh, J. Renew. Sustain. Energy 2 (2010) 42701–42738.
[10] M.A. Gondal, X.F. Chang, M.A. Ali, Z.H. Yamani, Q. Zhou, G.B. Ji, Appl. Catal. A – Gen. 397 (2011) 192–200.
[11] K. Byrappa, A.K. Subramani, S. Ananda, K.M.L. Rai, R. Dinesh, M. Yoshimura, Bull. Mater. Sci. 29 (2006) 433–438.
[12] P. Wilhelm, D. Stephan, J. Photochem. Photobiol. A – Chem. 185 (2007) 19–25.
[13] A.M. Asiri, M.S. Al-Amoudi, T.A. Al-Talhi, A.D. Al-Talhi, J. Saudi Chem. Soc. 15 (2011) 121–128.
[14] S.C. Yan, Z.S. Li, Z.G. Zou, Langmuir 26 (2010) 3894–3901.
[15] F. Qin, H.P. Zhao, G.F. Li, H. Yang, J. Li, R.M. Wang, Y.L. Liu, J.C. Hu, H.Z. Sun,

R. Chen, Nanoscale 6 (2014) 5402–5409.
[16] C.C. Chen, W. Zhao, P.X. Lei, J.C. Zhao, N. Serponer, Chem.-Eur. J. 10 (2004) 1956–1965.
[17] R.K. Wahi, W.W. Yu, Y.P. Liu, M.L. Mejia, J.C. Falkner, W. Nolte, V.L. Colvin, J. Mol. Catal. A – Chem. 242 (2005) 48–56.
[18] M.N. Rashed, A.A. El-Amin, Int. J. Phys. Sci. 2 (2007) 073–081.
[19] F. Qin, G.F. Li, H. Xiao, Z. Lu, H.Z. Sun, R. Chen, Dalton Trans. 41 (2012) 11263–11266.
[20] Z. Dai, F. Qin, H.P. Zhao, F. Tian, Y.L. Liu, R. Chen, Nanoscale 7 (2015) 11991–11999.
[21] J.Y. Xiong, G. Cheng, F. Qin, R.M. Wang, H.Z. Sun, R. Chen, Chem. Eng. J. 220 (2013) 228–236.
[22] Z.C. Shan, Y.M. Wang, H.M. Ding, F.Q. Huang, J. Mol. Catal. A – Chem. 302 (2009) 54–58.
[23] Y.X. Zhou, H.B. Yao, Q. Zhang, J.Y. Gong, S.J. Liu, S.H. Yu, Inorg. Chem. 48 (2009) 1082–1090.
[24] H.Y. He, J.F. Huang, L.Y. Cao, J.P. Wu, Desalination 252 (2010) 66–70.
[25] C.M. Li, G. Chen, J.X. Sun, H.J. Dong, Y. Wang, C. Lv, Appl. Catal. B – Environ. 160 (2014) 383–389.
[26] Y. Yan, Y.F. Wu, Y.T. Yan, W.S. Guan, W.D. Shi, J. Phys. Chem. C 117 (2013) 20017–20028.
[27] X. Ding, K. Zhao, L.Z. Zhang, Environ. Sci. Technol. 48 (2014) 5823–5831.
[28] Y.H. Zhang, N. Zhang, Z.R. Tang, Y.J. Xu, Chem. Sci. 4 (2013) 1820–1824.
[29] S. Helali, M.I. Polo-Lopez, P. Fernandez-Ibanez, B. Ohtani, F. Amano, S. Malato, C. Guillard, J. Photochem. Photobiol. A – Chem. 276 (2014) 31–40.
[30] H.C. Gupta, Archana, V. Luthra, J. Mol. Struct. 1005 (2011) 53–58.
[31] Z.Q. Li, X.T. Chen, Z.L. Xue, J. Colloid Interface Sci. 394 (2013) 69–77.
[32] X.J. Wang, X.L. Wan, L.L. Chang, Catal. Lett. 144 (2014) 1268–1277.
[33] Y.M. Liu, H.B. Tang, H. Lv, Z.J. Li, Z.W. Ding, S. Li, Ceram. Int. 40 (2014) 6203–6209.
[34] C.X. Xu, X. Wei, Z.H. Ren, Y. Wang, G. Xu, G. Shen, G.R. Han, Mater. Lett. 63 (2009) 2194–2197.
[35] W. Wei, J.M. Xie, X.M. Lu, P.B. Osei, Z.X. Yan, S.C. Meng, H.L. Cui, Mon. Chem. 145 (2014) 47–59.
[36] Z.J. Zhang, W.Z. Wang, M. Shang, W.Z. Yin, J. Hazard. Mater. 177 (2010) 1013–1018.
[37] Y.M. Cui, H.Q. Li, W.S. Hong, S.H. Fan, L.J. Zhu, Powder Technol. 247 (2013) 151–160.
[38] N.A. McDowell, K.S. Knight, P. Lightfoot, Chem.-Eur. J. 12 (2006) 1493–1499.
[39] M. Maczka, J. Hanuza, W. Paraguassu, A.G. Souza, P.T.C. Freire, J. Mendes, Appl. Phys. Lett. 92 (2008) 112911.
[40] M. Ptak, M. Maczka, K. Hermanowicz, A. Pikul, J. Hanuza, Spectrochim. Acta A Mol. Biomol. Spectrosc. 86 (2012) 85–92.
[41] M. Maczka, L. Macalik, K. Hermanowicz, L. Kepinski, P. Tomaszewski, J. Raman Spectrosc. 41 (2010) 1059–1066.
[42] P.R. Graves, G. Hua, S. Myhra, J.G. Thompson, J. Solid State Chem. 114 (1995) 112–122.
[43] M. Maczka, L. Macalik, S. Kojima, J. Phys. Condes. Matter 23 (2011) 405902.
[44] D.L. Wood, J. Tauc, Phys. Rev. B 5 (1972) 3144–3151.
[45] J.G. Solé, L.E. Bausá, D. Jaque, An Introduction to the Optical Spectroscopy of Inorganic Solids of Solids, in: John Wiley & Sons Ltd, San Francisco-USA, 2005.
[46] H.B. Fu, J. Lin, L.W. Zhang, Y.F. Zhu, Appl. Catal. A – Gen. 306 (2006) 58–67.
[47] A.B. Murphy, Sol. Energy Mater. Sol. Cells 91 (2007) 1326–1337.
[48] B. Ohtani, J. Photochem. Photobiol. C – Photochem. Rev. 11 (2010) 157–178.
[49] A. Singh, D.P. Dutta, M. Roy, A.K. Tyagi, M.H. Fulekar, J. Mater. Sci. 49 (2014) 2085–2097.
[50] T. Saison, P. Gras, N. Chemin, C. Chaneac, O. Durupthy, V. Brezova, C. Colbeau-Justin, J.P. Jolivet, J. Phys. Chem. C 117 (2013) 22656–22666.
[51] N. Daneshvar, D. Salari, A.R. Khataee, J. Photochem. Photobiol. A – Chem. 162 (2004) 317–322.
[52] S. Belaidi, T. Sehili, L. Mammeri, K. Djebbar, J. Photochem. Photobiol. A – Chem. 237 (2012) 31–37.
[53] J. Jiang, K. Zhao, X.Y. Xiao, L.Z. Zhang, J. Am. Chem. Soc. 134 (2012) 4473–4476.